Effect of Solution Aggressiveness on the Crack Growth Resistance and Cracking Mechanism of AA2024-T3

Christina Margarita Charalampidou[1], Christiaan C.E. Pretorius[2]; Roelf J. Mostert[2,*]; Nikolaos D. Alexopoulos[1,*]

[1]University of the Aegean, School of Engineering, Department of Financial Engineering, Research Unit of Advanced Materials, 821 32 Chios, Greece.

[2]University of Pretoria, Department of Material Sciences and Metallurgical Engineering, 395, Pretoria, Republic of South Africa.

*Corresponding authors. Email: Roelf.mostert@up.ac.za; nalexop@aegean.gr

Abstract

Aluminum alloy 2024-T3 was examined using a range of microscopy techniques at the early stages of corrosion attack to investigate the corrosion-induced cracking mechanism. Two different corrosive environments—exfoliation corrosion (EXCO) and 3.5 wt% NaCl—were used for the exposure of tensile and prenotched compact-tension C(T) specimens of AA2024-T3. Different embrittlement mechanisms are noticed for the two investigated corrosive environments. Significant intergranular corrosion (IGC) and grain boundary embrittlement are evident in the specimens exposed to EXCO solution, whilethis was not the case for the milder solution comprising of 3.5 wt% NaCl. With regard to the milder solution, the corrosion attack is not only restricted to the grain boundary, but evolves transgranularly to the neighboring grains of the IGC attacked region and, consequently, the grain boundary strength in the direct vicinity is not notably affected. The extent of secondary cracks, after the exposure of C(T) specimens to EXCO solution and the subsequent crack-growth resistance evaluation, were found to correlate with the diameter of the plastically affected zone (≈3.78±0.04 mm). Additionally, the depth of these cracks was found to correlate well with the thickness of the intergranular fracture surface, giving evidence that the secondary cracks form due to grain boundary embrittlement; probably attributed to hydrogen embrittlement phenomena.

Keywords: crack growth, exfoliation corrosion, fracture toughness, pitting corrosion

INTRODUCTION

The long-term usage of the widely used aluminum alloy 2024 in the aeronautical industry may lead to the degradation the alloy's mechanical performance during its service life. The degradation of the mechanical properties, such as tensile strength, fracture toughness, as well as elongation at fracture (ductility)—may be brought on by several mechanisms, including the natural aging of the alloy, intergranular corrosion, and hydrogen embrittlement (as well as their combined effects).[1-3] The improved mechanical properties of AA2024 are attributed to

its precipitation hardening system,[4] that follows the well-known sequence of supersaturated solid solution → Guinier-Preston-Bagaryatsky (GPB) zone / S'' → S' → S (Al_2CuMg) phase.[5] The S'' phase is a coherent ordering of Cu and Mg solutes, while the S phase is an incoherent, lath-shaped equilibrium phase that is formed at the over-aged condition. The coarsening of the precipitates in this condition leads to the loss in the precipitates' coherency with the aluminium matrix and, consequently, lowers the mechanical performance. Several approaches have been used to simulate the natural aging of aluminum alloys in the laboratory, which includes artificial ageing heat treatments to accelerate the microstructural transformations (e.g., Moy, et al.,[4-8]) and assess its effect on the mechanical properties. For example, Rong-Xian, et al.,[9] investigated the multistage-aging process effect on formation of GP zones and their effect on the mechanical properties. Alexopoulos, et al.,[10] showed a drastic effect on the yield stress and the elongation at fracture of AA2024-T3, with the former being essentially increased up to the peak-aging condition while elongation at fracture decreased due to the precipitation of the S-type particles. Additionally, a significant hardness improvement with increasing ageing time was shown in the work by Astika.[11] In Wang, et al.,[12] the effect of aging at 140°C on the tensile properties, microstructures and fractographies of AA2024, subjected to solutionizing followed by water quenching and room-temperature rolling with 80% thickness reduction, was studied. It was found that both the strength and ductility change with the precipitation of S'' and S phases and the subsequent decrease in dislocation density, but not with the grain and texture characteristics. Xu, et al.,[13] also performed similar investigations with interrupted aging treatments to assess the effect on the mechanical properties. Finally, Pakravan, et al.,[14] performed different artificial aging conditions to assess the effect of fracture behavior under tension. Tensile yield stress and elongation at fracture are considered important properties for the design of aircraft structures, and are usually considered as two contradictory mechanical properties for aluminum alloys. That is, the increase in strength often leads to a decrease in ductility and vice versa, nevertheless with several exceptions, e.g., by Zhao, et al.[15]

The presence of grain boundary precipitates and intermetallic particles (IMs) was found to increase the susceptibility of Al-Cu alloys to localized corrosion attack, such as intergranular corrosion (IGC).[16-18] Several articles in the open literature showed that the IGC dominant mechanism is the formation of a galvanic cell between the Cu-rich IMs precipitated on the grain boundaries, e.g., θ type (Al_2Cu) and S-type (Al_2CuMg) in case of AA2024, and the matrix or the adjacent Cu-depleted particles.[19-21] The anodic dissolution of the S-phase particles starts from the release of magnesium into the solution, which results in copper enrichment; therefore, particles become nobler than matrix, which leads to the dissolution of the surrounding matrix.[22] Among several types of localized corrosion attack mechanisms found in aeronautical aluminum alloys, the most common atmospheric corrosion mechanism is referred to as exfoliation corrosion (EXCO), and is caused by the exposure of these aluminum alloys to moist and/or corrosive environments. EXCO is considered as a particular form of intergranular corrosion attack that occurs on the corroded surfaces of aircraft structures comprising of elongated grain structures, e.g., Posada, et al.,[23] and Robinson and Jackson.[24] The ASTM G34 Standard[25] defines EXCO as corrosion that proceeds laterally along planes parallel to the surface—generally along grain boundaries—where it forms voluminous corrosion products that, due to internal stress formation, forces the metal apart. Despite the fact that studies regarding exfoliation corrosion in aluminium alloys started many decades ago, the crucial phenomena and mechanisms associated therewith remain unclear. Several papers in the open literature suggested that the exfoliation corrosion results either from intergranular corrosion or a stress corrosion cracking (SCC) mechanism.[26-28] However, the prominent mechanism of EXCO is still unclear.

Various studies on the corrosion behavior of Al-Cu alloys showed that exfoliation corrosion can lead to significant material degradation by reducing the ultimate tensile strength, fracture toughness, and fatigue endurance limit,[29-30] as well as accelerate fatigue crack growth rate.[31] A moderate degradation of the material's mechanical strength properties, e.g., yield stress and ultimate tensile strength, along with a significant reduction in the tensile ductility (i.e., elongation at fracture) was revealed from several studies regarding AA2024.[1,32-34] According to Alexopoulos and Papanikos,[1] the reduction of the specimens' load carrying cross section—referred to as "effective thickness"—as well as the notch effects caused by pitting formation are responsible for moderate reduction of the yield stress and ultimate tensile strength properties. Evolution of corrosion attack perpendicular to the surface up to a certain critical size was found by Alexopoulos, et al.,[34] where after a mixed mode of attack occurs. The authors further stated that this mixed mode attack consists of both intergranular corrosion and grain etch out (specifically near the *S*-phase precipitates), resulting in the lateral growth of the corrosion parallel to the rolling direction.

Important findings on the corrosion behavior of AA2024 revealed a recovery of the residual strength after the mechanical removal (e.g., by milling) of the corrosion layer; however, this was not the case for elongation at fracture.[35] This gave rise to the idea that the plasticity of the alloy is not only degraded by corrosion-induced cracking formation, but also a corrosion-induced mechanism of hydrogen embrittlement, as was examined by Kamoutsi, et al.[36] The destruction of the alloys' surface oxide film, either due to mechanical processes or due to corrosion, can lead to the absorption of hydrogen atoms into aluminum alloy.[37-39] During the corrosion process, atomic hydrogen is introduced to the alloy through the reduction of water (H_2O) according to the following dissociation process:[40]

$$H_2O \leftrightarrow OH^- + H^+ \quad (1)$$

where the atomic hydrogen may then either be absorbed into the aluminum matrix, or react on the surface to form hydrogen gas (H_2). In the former case, the atomic hydrogen will diffuse to certain preferred lattice sites, such as microstructural point-defects, line-defects/dislocations, grain-boundaries, and precipitates (including matrix/precipitate interfaces).[41-44] These lattice sites act as hydrogen traps, resulting in the embrittlement of the alloys through the conventional hydrogen-embrittlement mechanisms. Bond, et al.,[45] showed that the presence of hydrogen increases the mobility of dislocations during plastic deformation, resulting in highly localized plastic deformation and fracture. This phenomenon is usually referred in the literature as the hydrogen enhanced localized plasticity (HELP) mechanism.[46-47] Additionally, another mechanism of hydrogen embrittlement, called hydrogen enhanced decohesion (HEDE), also has been proposed.[48] HEDE is considered a reduction in the bonding strength between the metal atoms due to the presence of hydrogen. Several mechanisms of hydrogen embrittlement (HE) have been reported; nevertheless, there is no universally accepted HE mechanism. However, it is generally accepted that some critical concentrations of hydrogen can cause premature failure of the high-strength aluminum alloys. In more recent work by Alexopoulos, et al.,[49] it was found that the total decrease in the elongation at fracture was attributed to two different mechanisms: the first one consisted of the ¼ (actually 27%) of the total decrease in elongation at fracture and was attributed to the hydrogen embrittlement, while the remaining ¾ (actually 73%) was attributed to microcrack formation and evolution. Therefore, the partitioning of hydrogen inside the metal and its effect on the mechanical property degradation is of paramount importance for understanding the mechanisms associated with this type of attack, and to design alloys with improved corrosion resistance behavior. Nevertheless, to assess the effect

of hydrogen embrittlement it is required to distinguish and eliminate the effect of microcrack formation, because these two mechanisms usually act synergistically.

The focal point of the present work is to investigate the corrosion-induced cracking evolution mechanism of AA2024-T3 exposed to two different corrosive environments, with specific reference to the plastically affected zone at a crack. The crack formation and fracture mechanisms associated with exposure to the commonly used exfoliation corrosion solution (EXCO) are compared against that of the milder solution of 3.5 wt% NaCl with the aim of studying the differences in the corrosion-induced cracking mechanisms.

MATERIALS AND EXPERIMENTAL PROTOCOL

Materials

The material used in the current research is wrought 2024-T3 aluminum alloy, which was received in sheet form of 3.2 mm nominal thickness. The weight percentage chemical composition of the AA2024 alloy is 4.35% Cu, 1.50% Mg, 0.64% Mn, 0.50% Si, 0.10% Cr, 0.50% Fe, 0.25% Zn, 0.15% Ti, and Al rem. Tensile and fracture toughness compact tension (hereafter referred to as C(T)) specimens were machined from the longitudinal (L) rolling direction in accordance with the ASTM E8[50] and ASTM E561[51] standards, respectively. The geometrical dimensions were 12.5 mm × 3.2 mm at the reduced cross section, with a total length of 150 mm for the tensile specimens (refer to Figure 1). The C(T) specimens had a width (W) of 48 mm and an original notch length (a_n) of approximately 16.70 mm. Further machining of the received C(T) specimens included the preparation of a fatigue starter notch with smaller radius (approximately 0.12 mm), that was machined at the tip of the pre-existing notch root through EDM (refer to Figure 2[a]). Therefore, the notch length of the machined C(T) specimens became $a_n \approx 22.50$ mm. The alteration of the notch root radius was performed in order to reduce the deleterious effect of the large notch root radius on the initiation and propagation of the fatigue precrack.

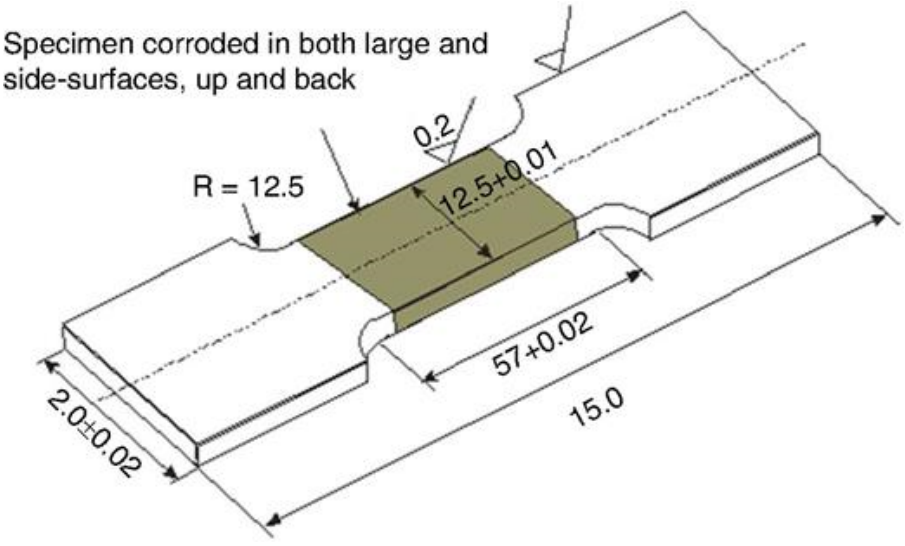

Figure 1. Schematic representation of shielded tensile specimens according to ASTM E8 specification.

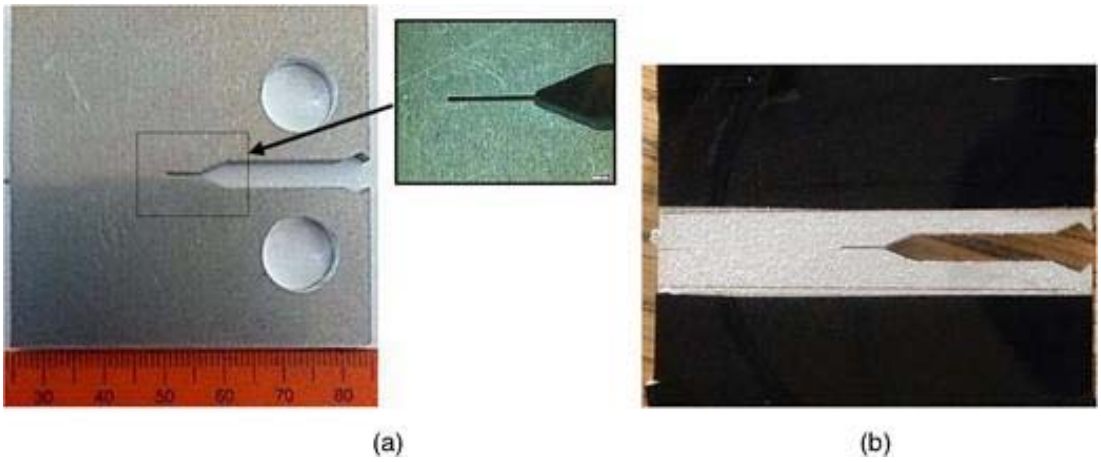

Figure 2. (a) Photograph of the C(T) specimens' geometry and notch detail according to ASTM E561 specification and (b) photograph of the shielded specimen.

Preparation of Corrosive Solutions

Prior to the corrosive solution exposure, the side-surfaces of the tensile specimens were polished up according to the ASTM E8[50] specification. Exposure of the test specimens to three different exposure environments were considered for this investigation. That is, (i) prior exposure to air for the baseline test results, (ii) prior exposure to a 0.6 M (or 3.5 wt%) NaCl solution with a pH within the range of 6.4 to 7.2 according to ASTM G44[52] specification, and (iii) prior exposure to EXCO solution according to ASTM G34[25] specification.

The 0.6 M NaCl exposure environment was prepared by adding 35.0 g of sodium-chloride (purity of 99.0% min) to 500 mL of distilled water and the pH measured at 8.25. The addition of the sodium-chloride to the distilled water reduced the measured pH from 8.25 to 7.65 after allowing enough time for the full dissolution of the sodium-chloride. To ensure that the pH value is between the established range of 6.4 to 7.2, a buffer solution containing hydrochloric acid with a pH value of 2.1 was prepared. Thereafter, approximately 0.05 mL of the buffer solution was slowly added to the sodium-chloride solution, lowering the measured pH of the solution to 6.14. An additional 500 mL of distilled water (pH measured at 8.25) was added to the sodium-chloride solution before transferring the solution into a storage container. The measured pH of the solution stabilized at 6.5 after allowing sufficient time for equilibrium to set in.

The exfoliation corrosion (EXCO) exposure environment is a solution consisting of approximately 4.0 M sodium-chloride (NaCl), 0.5 M potassium-nitrate (KNO_3), and 0.1 M nitric acid (HNO_3). The solution was prepared in accordance with ASTM G34 standard.[25] The preparation of the EXCO solution commenced with the addition of 50 g of potassium nitrate (reagent grade KNO_3 with 99.0 % purity) and 234 g sodium chloride (reagent grade NaCl with 99.0% purity) to 1 L of distilled water with measured pH at 8.25. After the addition of the reagents, the pH of the solution was measured at 7.58. According to the ASTM G34 standard, an additional 6.3 mL of 70% concentrated nitric acid (HNO_3) should have been added to the solution. However, due to the unavailability of a 70% concentrated nitric acid solution, the volumetric addition of the nitric acid was altered to make use of a 55% concentrated solution. Therefore, 8.5 mL of the 55% concentrated nitric-acid solution was added to the solution in order to obtain the required HNO_3 molarity. The solution was then

transferred to a proper storage container, and given sufficient time for equilibrium to set in. The final pH of the solution was measured at 0.27.

Prior Exposure of Specimens to Corrosive Solutions

Further specimen preparation was required prior to the exposure of the specimens to the relevant exposure environments. The preparation included shielding of the specimens' surfaces so that only specific areas of interest were exposed. Regarding the tensile specimens, masking with appropriate insulating PVC tape (with excellent adherence) was performed in order to avoid crevice corrosion beneath the masking tape. The exposed area was within the reduced cross section to ensure fracture within the gage length, as depicted in Figure 1. The C(T) specimens were shielded in such a way to ensure that only a 10 mm wide section near the specimen notch/precrack configuration would be exposed to the relevant exposure environments; in accordance with the ASTM E1681[53] specification, the environmental chamber should enclose the portion of the specimen that contains the crack tip. The shielding procedure consisted of measuring the relevant specimen dimensions (i.e., W, B and a_0) according to the ASTM E561 specification before covering the relevant surface areas with a layer of double-sided tape (refer to Figure 2[b]). Thereafter, the taped areas were covered again with a double layer of adherent PVC tape.

Fatigue precracking commenced on the C(T) specimens, prior to the corrosion exposure, using an Instron 1342† Servo-Hydraulic Testing Machine operating on Instron Crack Propagation† Software. The specimens were installed into the testing machine using the prescribed grips and fixtures in accordance with the ASTM E1820 standard.[54] The software was programed to cyclically strain the specimens at a constant stress intensity range (ΔK) of between 15 MPa√m and 27 MPa√m and a stress ratio (R) of 0.1. These cyclic loads were introduced until a fatigue precrack in the order of 2 mm was produced.

The solution volume was calculated per exposure area of the specimens: 10 mL/cm^2 for all specimens, both tensile and C(T), in accordance to the ASTM G34 standard. The specimens were then placed into the containers and allowed to be exposed for 2 h (hereafter referred to as 2 h) in EXCO solution and 24 h (hereafter referred to as 24 h) in 3.5 wt% NaCl solution. The 2 h exposure to EXCO solution was selected for further investigation because no essential stress decrease is noticed from the tensile flow curves, while a significant ductility decrease is evident (as was found in Alexopoulos, et al.[2]). The same is noticed in Alexopoulos, et al.,[55] for the 24 h exposure in the NaCl solution that was selected for further investigation. The specimens were removed and cleaned with acetone before performing the mechanical testing. Throughout the duration of the exposure the solutions were kept in 25±3°C temperature. At least three specimens in each test series were used for the reproducibility of the results.

Tensile Test Procedure

The tensile properties of the specimens were evaluated using an MTS Criterion 45 Static Testing Machine operating on MTS Elite Test Suite† software. The software was programmed to apply a tensile strain to the specimen—under crosshead displacement control—at a rate of 0.3 mm/min. The relevant specimen dimensions (i.e., the thickness t_0, width b_0, and gauge length L_0) were then taken and programed into the software. Thereafter, the specimens were individually installed into the MTS V-grips, ensuring good alignment with the loading axis. An extensometer of 50 mm initial gauge length was installed onto the

specimens and zeroed before applying a 1 kN preload to the specimen. The test was then allowed to commence, with termination set to occur after the complete fracture of the specimens. After the termination of the tests, the relevant specimen dimensions were measured again and tabulated. The raw data from each test was then analyzed using a specially programmed Excel spreadsheet and edited with the aid of Microcal Origin©† software. Additionally, some of the tensile tests were interupted after the introduction of a certain engineering strain—up to 2%—and their surfaces were microscopically analyzed. The prestraining process was performed to examine the intergranular cracking mechanism at low engineering strains, without the effect of excessive straining due to tensile loading.

Crack Growth Resistance Test Procedure

The crack growth resistance evaluation was performed using an MTS Criterion 45 Static Testing Machine operating on MTS Elite Test Suite software. The software was programed to strain the specimen crack mouth opening under crosshead displacement control at a constant displacement rate of 0.03 mm/min. As per the unloading compliance method of the ASTM E561 standard, the software was programed to introduce a number of unloading/reloading sequences during each test. The specimens were installed into the test machine using the proper grips and fixtures, as prescribed in the ASTM E1820 standard.[54] Before testing commenced, the CMOD gauge extensometer was zeroed using a reference specimen with an initial crack mouth opening of 5.0 mm. The CMOD gauge was then installed onto the specimen and a small preload of 0.2 kN was applied in order to ensure good alignment of the specimen with the test machine's loading axis. The test was set to terminate once a CMOD of 3 mm was achieved. After the termination of the test, the specimens were subjected to a final high strain rate loading (crosshead-displacement rate of 300 mm/min) until the complete separation of the specimen. The specimen was then removed from the grips before measuring the initial and final crack lengths using a stereo microscope. In some cases, the deliberate staining of the specimen crack—with black ink—prior to the final separation of the specimen was performed to establish an accurate understanding of the various fracture surface appearances that comprise of the final crack length. The crack extension values were determined from the compliance curves, using the initial and final crack length measurements as calibration.

An alteration to the overall crack growth resistance test procedure was performed for some specimens regarding the final separation (full fracture) step, as well as the final crack length measurement. That is, after the termination of the test at a crack-mouth-opening-displacement of 3 mm, the specimens were removed from the grips. The post-test specimens were then sent for EDM in order to section out specimens for x-ray computed microtomography imaging (micro-XCT) containing the entirety of the newly produced crack and adjacent specimen surfaces. The micro-XCT specimens were then scanned to obtain 3D images of the specimen and cracks, with the purpose of investigating the extensive secondary cracking that could be observed parallel to and in front of the main crack on the EXCO exposed specimen surfaces after K_R testing. A specimen examined in this way is depicted in Figures 13 and 14, referred to as specimen B2.

RESULTS AND DISCUSSION

Effect of Corrosion Exposure on the Tensile Mechanical Properties

Typical tensile curves of the pre-corroded specimens of AA2024-T3 exposed to an EXCO solution and a 3.5 wt% NaCl solution are presented in Figures 3(a) and (b), respectively (as presented in Alexopoulos, et al.,[2,55] respectively). The nominal stress calculation was based on the nominal cross section of the tensile specimens, namely, width × thickness = 12.5 mm × 3.2 mm. The tensile flow curves are presented for the justification of the selected corrosion exposure times in the current investigation, i.e., 2 h to the EXCO solution, and 24 h to the NaCl solution, respectively. The prior exposure of AA2024-T3 to the EXCO solution revealed significant alterations to the overall tensile mechanical properties of the alloy. It is apparent from Figure 3(a) that an overall reduction in plasticity is obtained after the exposure of the alloy to the EXCO solution. Despite the fact that the values of the conventional yield stress ($R_{p0.2\%}$) and the ultimate tensile strength (R_{UTS}) are not notably influenced by corrosion exposure for the short exposure times (up until 2 h), a notable ductility decrease is evident even after 0.5 h of exposure, which is attributed to the hydrogen embrittlement phenomenon. Similar results were found in Bond, et al.,[45] in which dislocation movement was significantly accelerated even after short exposure times, i.e., 14 s in 20 torr H_2/H_20, leading to hydrogen enhanced localized plasticity (HELP). Additionally, according to Birnbaum and Sofronis,[46] macroscopic hydrogen decreases have been observed at very low strain rates, and when hydrogen was introduced under conditions which did not cause any structural damage to the specimens, such as in very short exposure times. After 4 h corrosion exposure time to the EXCO solution, a significant stress drop is noticed, which is attributed to the decrease of the specimen's "effective thickness" according to a previous study of the authors.[1] Therefore, the 2 h exposure time to the EXCO solution was selected for further investigation of the corrosion-induced cracking mechanism, because the slight pitting formation does not notably influence the effective thickness of the specimen.

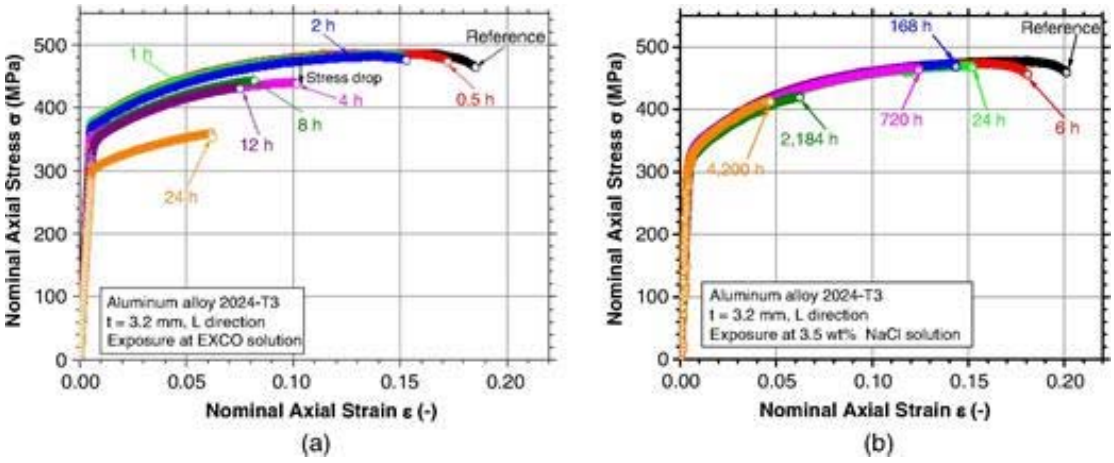

Figure 3. Typical tensile nominal stress-strain curves of AA2024-T3 after corrosion exposure to (a) EXCO solution and (b) 3.5 wt% NaCl solution.

The prior exposure of AA2024-T3 specimens to 3.5 wt% NaCl solution revealed no significant changes with regards to the yield stress and the ultimate tensile strength; even for the highest exposure time of 4,200 h (refer to Figure 3[b]). However, a notable decrease in the elongation at fracture A_f of the material is observed; reducing from the baseline average

of 19±0.3% to 15.2% after only 24 h exposure time. An even higher degradation in the A_f was observed at exposure time in the range of 6 h and 168 h, where pitting incubation takes place, as well as in the time range of 720 h and 2,184 h, probably because of the change in the degradation mechanism towards pit growth and coalescence. Signs of localized corrosion throughout the grain boundary network of AA2024-T351 were evident from the significant increase in corrosion volume between 96 h and 168 h of exposure to NaCl solution, as revealed by Knight, et al.[56] Thus, the 24 h exposure time—where the pitting formation takes place—was selected by the authors for further investigation. Additionally, it is apparent from the figure that the elastic and plastic portions of both the unexposed (baseline) and prior-exposed specimens are very similar up to the point of necking (or the R_{UTS}). However, for the exposed specimens, fracture essentially ensues immediately after the necking sets in.

A significant amount of intergranular tearing was observed by the micro-XCT imaging on the surfaces of the post-test tensile specimens exposed to the EXCO solution, as can be seen in Figure 4. Several secondary cracks (intergranular tears) have formed perpendicular to the loading direction due to grain boundary embrittlement. The corrosion products between the grain layers tend to expand with corrosion evolution and act as wedges that introduce a stress field, thereby accelerating the formation of in-plane intergranular cracks.[23] Formation of some surface pits after 2 h exposure to the EXCO solution is evident from the cross section in Figure 4(c), where the pits seem not to propagate deeply into the core of the material, but parallel to the surface. Furthermore, higher pitting density is noticed in the L/ST direction (z-y plane axis), providing evidence that the side-surfaces of the specimens are more prone to corrosion attack, as was experimentally observed from Kamoutsi[57] and Pantelakis, et al.,[58] thus playing a pivotal role in the A_f degradation at these short exposure times, as was also revealed by Charalampidou, et al.[59]

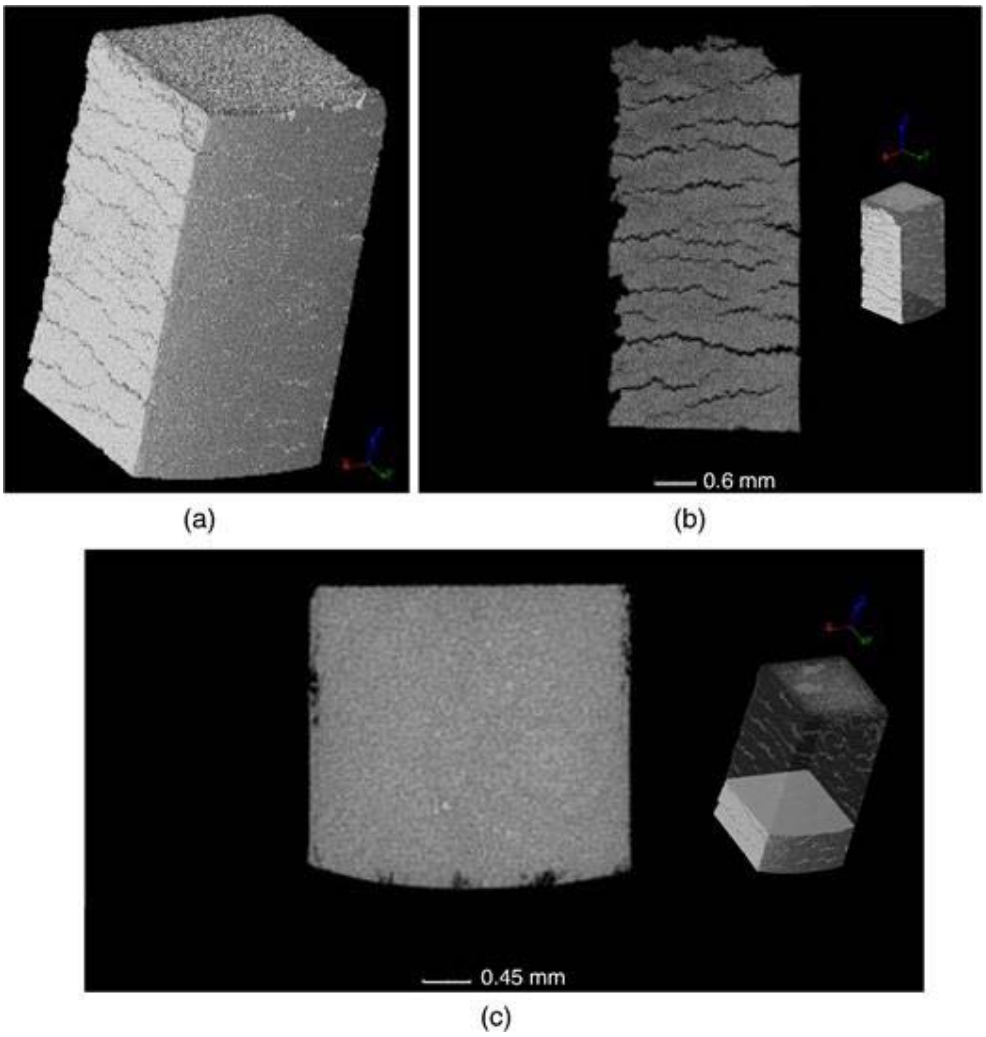

Figure 4. Post-tensile test micro-XCT images of the EXCO-exposed specimens, with (a) full-volume micro-XCT specimen, (b) a section near the exposed surface showing the intergranular tearing due to grain-boundary embrittlement, and (c) the cross-sectioned area shown in the right image included.

In order to develop an understanding regarding the development of these cracks, micro-XCT imaging was also performed on a tensile tested specimen, in which the test was interrupted after the application of 2% engineering strain. The micro-XCT image shown in Figure 5(a) reveals that, even at these low engineering strains, intergranular cracking is present with an approximate depth of 0.05 mm (50 μm) into the specimen (refer to Figure 5[b]). Similar intergranular corrosion penetration was found in Hughes, et al.,[60] after 2 h exposure of AA2024-T3 to 0.1 M NaCl solution. Additionally, approximately 40 μm depth of cracks was noticed in Alexopoulos, et al.,[2] after 4 h exposure to EXCO solution and without the application of prior engineering strain. Notable intergranular cracking was observed to propagate deep into the metal prior to the formation of any substantial surface pitting. The same was noticed in the work of Luo, et al.,[61] where the intergranular corrosion attack of AA2024-T351 was microscopically examined after immersion in 0.1 M NaCl aqueous solution.

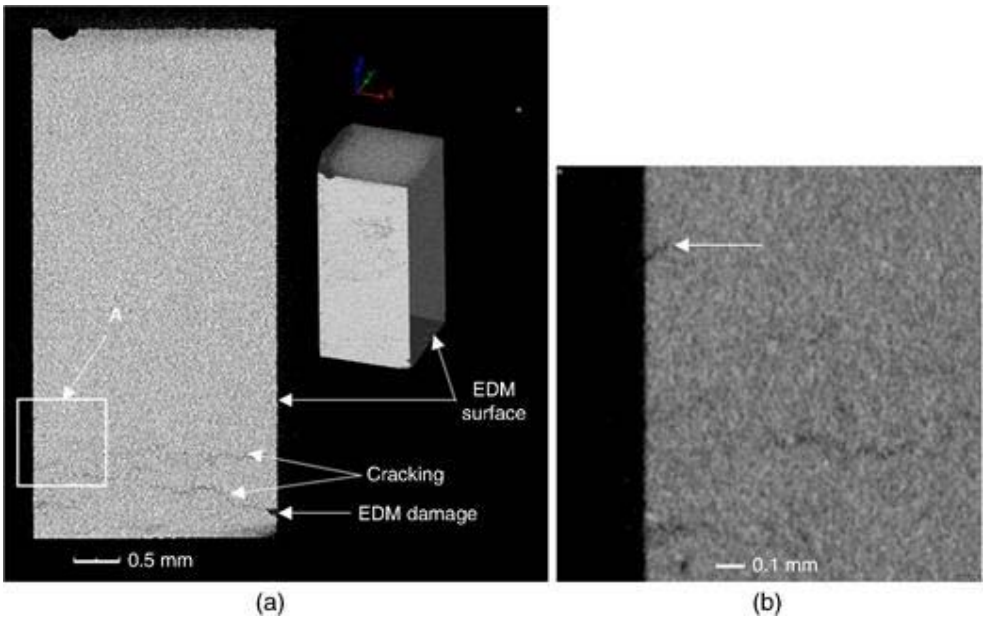

Figure 5. (a) Micro-XRCT image of 2 h EXCO exposed AA2024-T3 tensile specimen after the application of 2% engineering strain and (b) higher magnification of section A, showing that the secondary cracking extends to an approximate depth of 0.05 mm from the exposed surface.

Macroscopic Features of Corrosion Exposure

Optical microscopy of the NaCl-exposed C(T) specimens—prior to the crack-growth resistance evaluation revealed indications of localized corrosion attack in the form of pitting and intergranular corrosion. During the 24 h exposure of the specimens to 3.5 wt% NaCl solution, a significant amount of precipitation in the form of a solid white layer of pustules was observed on the exposed surfaces, as can be seen in Figure 6(a). In Figure 6(b), the observed localized corrosion attack appears to be more concentrated within the regions where the solid white layer of pustules has formed. Concerning the basic mechanism of pitting corrosion, Vargel[62] defines the overall reaction for pitting corrosion of aluminum alloys as:

$$2Al + 3H_2O + \frac{3}{2}O_2 \rightarrow 2Al(OH)_3 \qquad (2)$$

Figure 6. (a) Photograph showing the white precipitate layer on the specimens surface after 24 h immersion in the 3.5 wt% NaCl solution and (b) optical micrograph (200× magnification) showing the significant pitting and intergranular attack within the area where white layer (Al(OH)3) formation occurred.

Therefore, the solid white layer is believed to be the precipitation of aluminium-hydroxide $Al(OH)_3$, which results from corrosion of the aluminum. The dissolution of aluminum at the pit's bottom leads to high concentration of Al^{3+}, which later diffuse toward the pit's opening. The half reaction concerned with the reduction of water or hydrogen (H^+) at the cathodic regions outside the pit is expected to result in localized excess of OH^- at these sites, thereby increasing the pH (measured pH of 6.5) and, consequently, the alkalinity of the solution near these regions,[62] thereby giving rise to the precipitation of aluminum-hydroxide. It is also observed that, once the specimen is moved, the solid white layer dissolves again. The dissolution of the white layer may be explained by the dissolution of aluminum-hydroxide after being exposed to the acidic environment (lower measured pH) of the bulk solution; this is in accordance to the findings of Gayer, et al.[63]

During the 2 h exposure of AA2024-T3 C(T)-specimens to the EXCO solution, extensive bubble formation could be observed on the exposed surfaces (Figure 7). Considering the measured pH of the solution (0.27) and the basic moddel for pitting corrosion of aluminum,[62] the gas bubbles are believed to be hydrogen that forms as a result of the reduction of protons (H^+) in acidic solution according to Reaction (3). The necessary electrons for the formation of the hydrogen gas (H_2) are provided by the oxidation of the aluminium according to Reaction (4):

$$6H^+ + 6e^- \rightarrow 3H_2 \qquad (3)$$

$$2Al \rightarrow 2Al^{3+} + 6e^- \qquad (4)$$

Figure 7. Hydrogen bubble formation during EXCO exposure after (a) 15 min, (b) 30 min, and (c) 90 min.

The hydrogen gas-bubble formation was also accompanied by the precipitation of a large amount of small, cubic-shaped salt crystals with a white coloration which can be attributed to precipitation of sodium-chloride (NaCl) or aluminum-chloride ($AlCl_3$). However, SEM evaluation of the specimen surfaces after the exposure to the EXCO solution revealed no visual signs of significant pitting nor intergranular corrosion (refer to Figure 8).

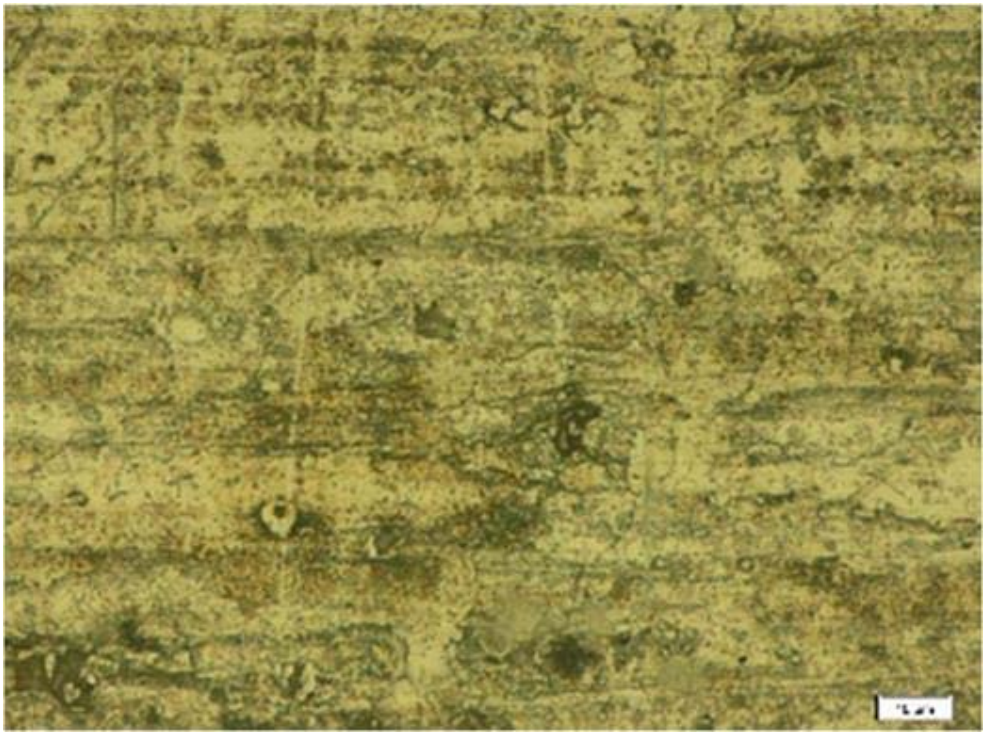

Figure 8. High-magnification (1,000×) optical micrograph of the C(T) (L-T) specimen surface after the 2 h exposure to the EXCO solution, showing no signs of significant pitting or intergranular corrosion.

Effect of Corrosion on Crack Growth Resistance Behavior

Figure 9(a) shows the load-crack mouth opening displacement (CMOD) curves and Figure 9(b) tabulates the evaluated critical stress intensity factor K_{cr} values (calculated from environmentally affected *R*-curves) of AA2024-T3 specimens exposed to three different exposure environments, that is (i) prior exposure to air for the reference test results, (ii) prior exposure to 0.6 M-(or 3.5 wt%) NaCl solution, and (iii) prior exposure to EXCO solution. As expected, the resistance curve is more recessive for the specimens exposed to corrosive environments (environmentally affected *R*-curve) regarding the maximum applied load and the associated critical crack extension values (Δa_c = 6.14 mm, 5.52 mm, and 5.26 mm for samples exposed to air, EXCO solution and NaCl solution, respectively). However, no significant difference in maximum applied load is noticed between the two corrosive environments. A bigger difference is evident when comparing the specimens exposed in air against the specimens exposed to corrosive solutions, than comparing the results in the two corrosive solutions. Specimens exposed in air were found to have a maximum load of approximately 4.0 kN, while specimens exposed to EXCO as well as to NaCl solution exhibited a maximum applied force of 3.8 kN and 3.7 kN, respectively. Regarding the CMOD at maximum load, no considerable difference is noticed between the three investigated cases. Hence, it seems that the short corrosion exposure times investigated in this study does not drastically affect the maximum load capacity of specimens as well as the CMOD at the maximum load. Nevertheless, a considerable decrease in the material's ability to resist the propagation of a pre-existing crack is noticed from the K_{cr} values in Figure 9(b), as well as the critical values of crack extension leading to instability, quoted above. Exposure of specimens to EXCO solution decrease the critical stress intensity factor K_{cr} by approximately 11%, while the respective decrease for NaCl-exposed specimens is

approximately 13%. Nevertheless, no signs of significant pitting nor intergranular corrosion observed in the surfaces of EXCO-exposed specimens, when evaluated with the aid of OM as shown in Figure 8.

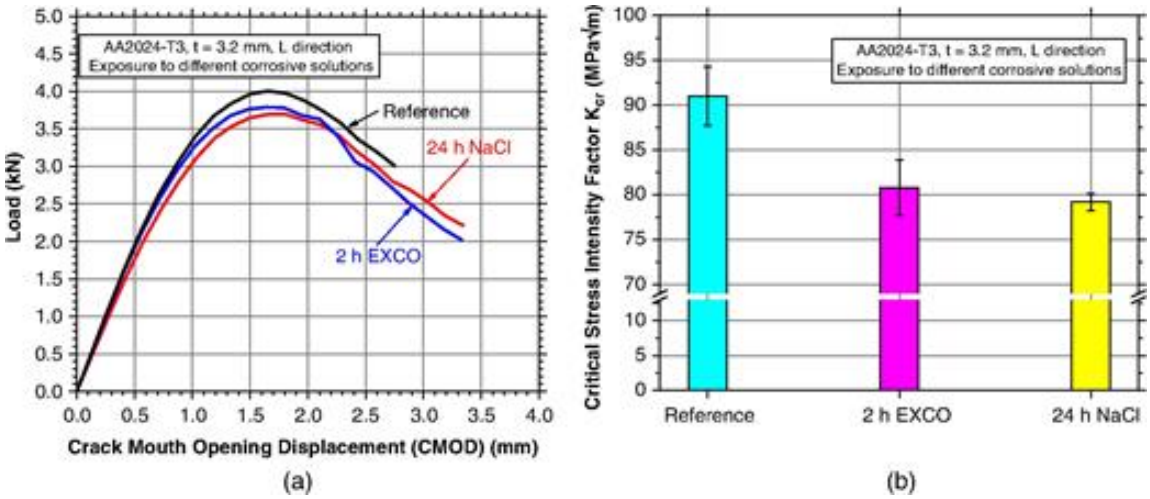

Figure 9. (a) Load-CMOD curves and (b) evaluated critical stress intensity factor (Kcr) values of AA2024-T3 specimens after prior exposure to different corrosive solution.

Figure 10 shows the captured SEM images of the NaCl-exposed C(T) specimen after the crack-growth resistance evaluation. A ductile fracture surface, labeled with C in Figure 10(a), immediately adjacent to the specimen outer surface (labeled with B) is evident from the dimples. Additionally, intergranular corrosion attack was revealed, as shown in the area labeled with D in Figure 10(a). It is evident from the dimpled fracture surface appearance, shown in higher magnification in Figure 10(b), that the crack propagated transgranularly. Furthermore, this transgranular crack propagation also persisted in the material near the intergranular attacked region. Similar observations have been reported in the literature;[64] revealing that intergranular corrosion attack is not restricted to the grain boundary itself, but tends to develop further in the interior of adgacent grains with high stored energy levels, thus becoming transgranular. This indicates that the type of corrosion mechanism brought on by the exposure of the AA2024-T3 to a solution containing purely sodium-chloride does not result in the significant grain-boundary embrittlement of the bulk material; as was the case for the specimens exposed to EXCO solution shown by Posada, et al.[23] The mechanism of embrittlement for EXCO-exposed specimens appears to deviate from that of the NaCl-exposed specimens. The grain boundary weakening appears to be limited to the regions where localized corrosion has occurred, with the grain boundary strength of the material in the direct vicinity of attacked regions not being affected fundamentally. This is in accordance with the low K_{cr} decrease noticed from the mechanical tests in Figure 9(b).

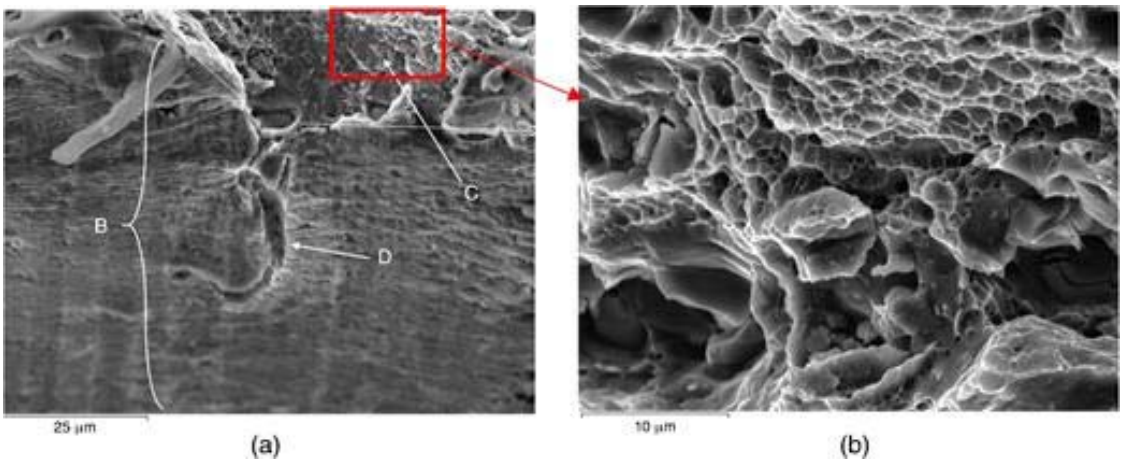

Figure 10. (a) SEM image near the surface (B until dashed lines) of the NaCl exposed specimen, showing the ductile (dimpled) fracture surface (C) immediately adjacent to the specimen surface, with (D) the point where intergranular corrosion has occurred and (b) higher magnification.

The fracture surface appearance of a specimen exposed to EXCO solution and after the crack-growth resistance evaluation is shown in Figure 11. As can be seen from the figure, the fracture surface can be divided into four different stages. That is the fatigue precrack perpendicular to the applied load marked with (A), the stable crack extension fracture surface perpendicular to the applied load (B), the shear-lip (ductile) fracture surface with an orientation of ±45° to the applied load (marked with [C]), and (D) an intergranular type of fracture near the edge of the specimen. It is worth noticing that the fracture surface types (A) to (C) are repeated in all exposure conditions considered for this investigation. However, only the EXCO-exposed specimens reveal the type (D) fracture surface appearance, corresponding to intergranular cracking.

Figure 11. Optical micrograph showing the typical fracture surface of the EXCO-exposed specimens, with (A) the fatigue pre-crack, (B) the stable crack extension, (C) shear-lip (ductile) fracture, and (D) intergranular fracture.

The SEM image in Figure 12 more clearly shows the intergranular fracture (D) of the material near the exposed surface (E) of the EXCO-exposed AA2024-T3 specimen. The presence of the intergranular fracture surface indicates the weakening of the grain boundary strength, as was revealed in previous studies (e.g., Posada, et al.[23]). It is also noteworthy to mention that the embrittlement appears to be more severe during exposure conditions in which the hydrogen gas do not evolve from exposed surface as readily. It has been noticed that exposure conditions in which the hydrogen bubbles remain adsorbed to the specimen surface reveal less pitting corrosion, higher concentration of precipitated salt, and a significant increase in the thickness of the intergranular fracture surface.

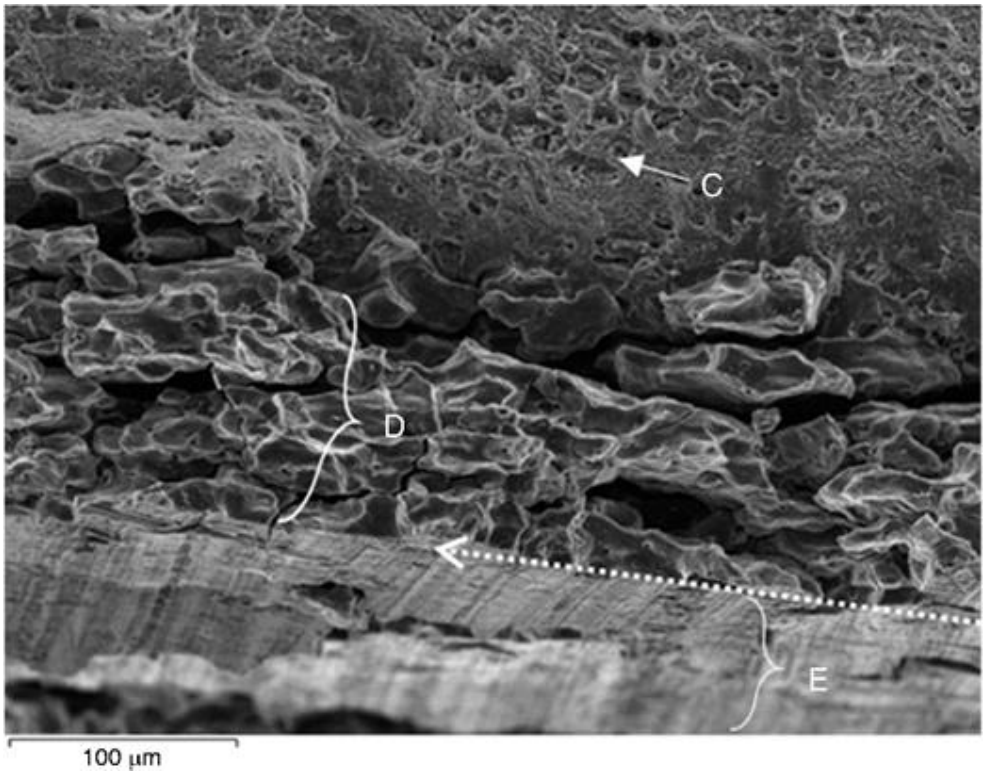

Figure 12. SEM image of the post crack-growth resistance evaluation fracture surface (D) near the exposed surface (E) of the EXCO-exposed C(T) (L-R) specimens.

Significant secondary crack formation adjacent to the primary crack is also observed after the crack-growth resistance evaluation of the EXCO-exposed specimens as can be seen in Figure 13. These secondary cracks do not form in the full width of the exposed region, but are limited to approximately 2 mm on either side of the main crack plane. Moreover, at a position of approximately 4 mm ahead of the extended primary crack front, no secondary cracks are observed. It is also important to note that the secondary cracks were not visible immediately after the exposure to the EXCO-solution (refer to Figure 8), but only formed after the crack-growth resistance testing, that is, after the loading of the specimens. Considering the plastic-zone size (r_y) calculated during the crack-growth resistance procedure (according to the ASTM E561 specification[51]), it appears that the final calculated diameter of the plastically affected zone (≈3.78±0.04 mm) correlates well with the area in which secondary crack formation is observed. Furthermore, according to the scale in Figure 14, the secondary cracks indicated with the red arrow (b) were measured through Image Analysis[†] software and found to extend up to an approximate depth of 0.115 mm from the exposed surface. This

corresponds well with the thickness of the intergranular fracture surface—labeled (D) in Figure 12, which was calculated to be 0.12 mm deep. The comparability between the depth of the secondary cracks evident in the EXCO-exposed specimens and the thickness of the intergranular fracture surface indicates that the secondary cracks form due to some form of grain boundary embrittlement. Whether this is induced by hydrogen embrittlement (HEDE model), or by the formation of some intergranular compound (e.g., AlH_3) during the exposure of the specimen, is yet to be determined. However, the cohesion strength of the grain boundaries near the exposed surface is significantly reduced.

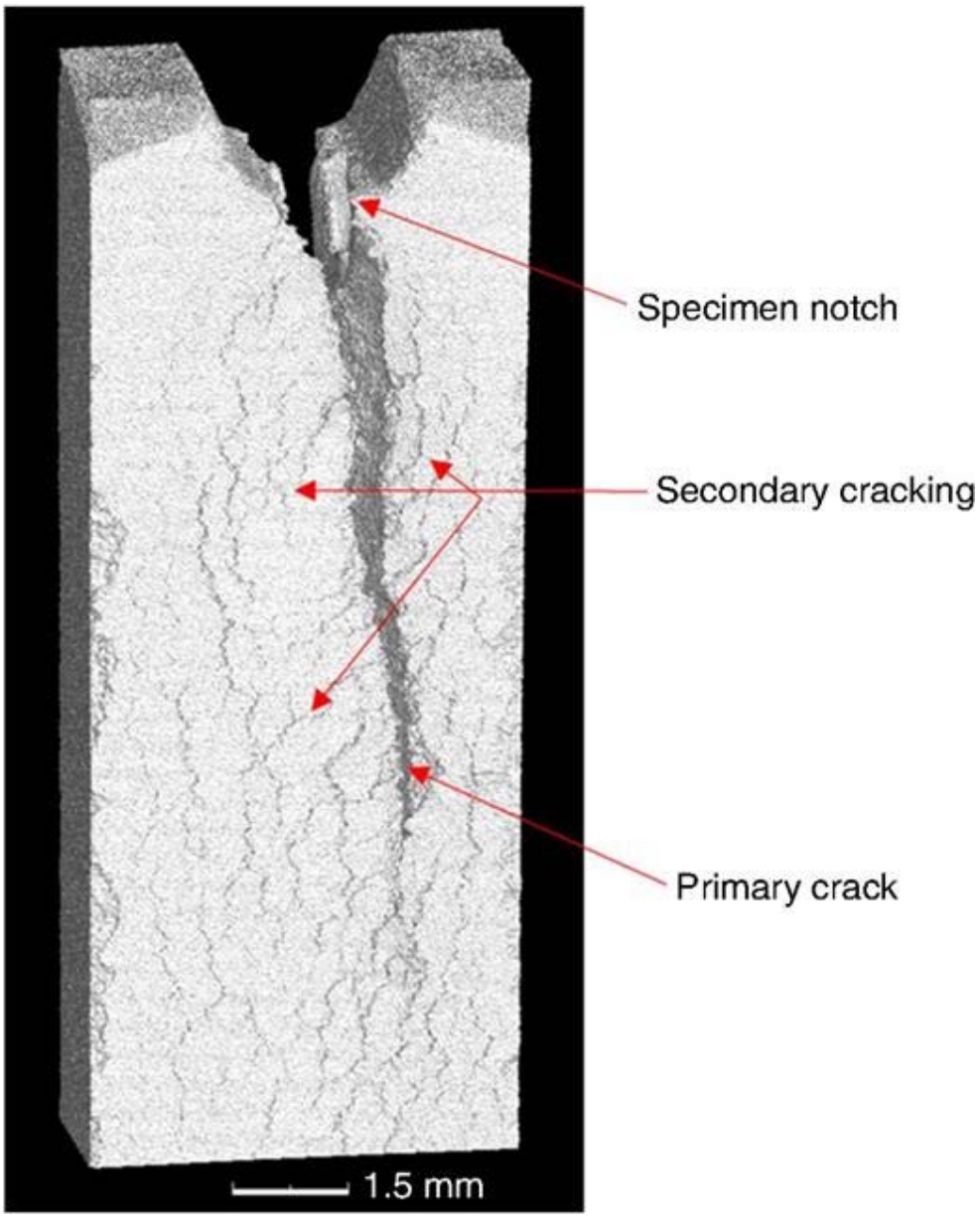

Figure 13. Post crack-growth resistance XCT image of the EXCO-exposed specimen B2, showing the secondary cracks that formed within the plastic zone near the primary crack front.

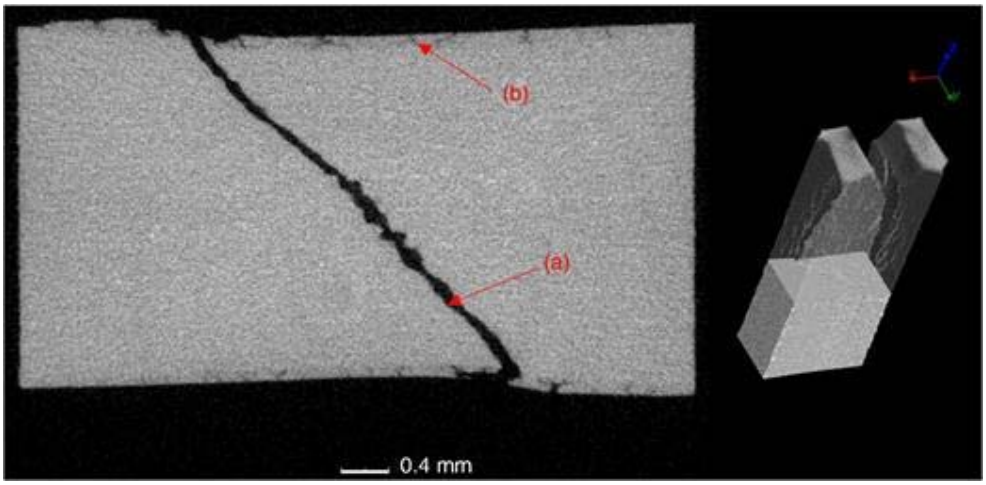

Figure 14. Post crack-growth resistance XCT images of the EXCO-exposed specimen B2, with the left image showing the (a) primary and (b) secondary cracks and the cross-sectioned area shown in the right image.

Furthermore, the loss in strength of the surface material also reduces the effective volume fraction of material with the ability to absorb the applied energy by yielding plastically. That is, the effective thickness of the specimen is reduced, and is smaller than the measured thickness used in the K_R calculations.

CONCLUSIONS

In the present study, the corrosion-induced cracking mechanism of AA2024-T3 in two different corrosive environments is investigated. Additionally, an attempt to calculate the plastically affected zone of the exposed materials is made and the following conclusions can be achieved.

Intergranular corrosion and grain boundary embrittlement are evident in the specimens exposed to EXCO solution. Approximately 50 μm intergranular cracking depth is revealed by examination of tensile specimens of AA2024-T3 when exposed to EXCO solution for short times and prior to the formation of any substantial surface pitting.

Extensive hydrogen gas (H_2)-bubble formation accompanied by the precipitation of a large amount of small, cubic-shaped salt crystals is revealed after 2 h EXCO exposure of AA2024-T3. However, no visual signs of significant pitting nor intergranular corrosion is evident in the area where bubbles were formed.

Approximately 11% of a decrease of the critical stress intensity factor K_{cr} is noticed for the specimens exposed to EXCO solution, while the respective decrease for the specimens exposed to 3.5 wt% NaCl solution is approximately 13%. Thus, the material's ability to resist the propagation of a pre-existing crack is similar after exposure to both solutions.

Signs of intergranular attack are also observed in the specimens exposed to 3.5 wt% NaCl solution; however, IGC is not restricted to the grain boundary itself, but tends to develop transgranularly to the adgacent grains of the intergranularly attacked region.

Different embrittlement mechanisms are noticed for the two investigated corrosive environments. No grain-boundary embrittlement is noticed for NaCl-exposed specimens while severe embrittlement is evident during exposure conditions in which the hydrogen gas do not evolve from exposed surface as readily but remains adsorbed to the specimen surface, as was the case for the EXCO-exposed specimens.

Several secondary surface cracks parallel to, and up to a distance of approximately 4 mm ahead of the extended primary crack front are observed after the crack growth evaluation on the EXCO-exposed specimens. This observation correlates well with the calculated plastically affected zone of approximately 3.78 mm.

The depth of secondary cracks was found to be approximately 0.115 mm and correlates well with the thickness of the intergranular fracture surface, which was found to be approximately 0.12 mm. Thus, it gives evidence that the secondary cracks form due to some form of grain boundary embrittlement.

ACKNOWLEDGMENTS

The micro-XCT work was performed by Prof. Anton van Niekerk's group at Stellenbosch University. Dr. Shatish Ramjee's assistance with the exposure testing is gratefully acknowledged. The financial assistance of the South African Department of Science and Innovation's Light Metal Development Network is gratefully acknowledged.

AUTHOR CONTRIBUTIONS

Conceptualization: N.D.A. and R.J.M.; experimental work: C.M.C. and C.C.E.P.; validation: N.D.A., R.J.M., C.C.E.P., and C.M.C.; writing-original draft preparation: C.M.C. and C.C.E.P.; writing – review and editing: N.D.A. and R.J.M.; supervision: N.D.A. and R.J.M. All authors read and approved the manuscript.

REFERENCES

1. N.D. Alexopoulos, P. Papanikos, Mater. Sci. Eng. A 498 (2008): p. 248-257.
2. N.D. Alexopoulos, Z. Velonaki, C.I. Stergiou, S.K. Kourkoulis, Corros. Sci. 102 (2016): p. 413-424.
3. B. Abdessamad, F. Jamel, B. Benattou, J. Fail. Anal. Prevent. 20 (2020): p. 197-207.
4. C.K.S. Moy, M. Weiss, J. Xia, G. Sha, Mater. Sci. Eng. A 552 (2012): p. 48-60.
5. Y.A. Bagaryatsky, Dokl. Akad. SSSR 87 (1952): p. 397-559.
6. J.R. Davis, ed., ASM Specialty Handbook: Aluminum and Aluminum Alloys (Metals Park, OH: ASM International, 1993).
7. J.W. Martin, Precipitation Hardening, 2nd ed. (Oxford, United Kingdom: Butterworth-Heinemann, 1998).
8. N. Radutoiu, J. Alexis, L. Lacroix, M. Abrudeanu, J.-A. Petit, Key Eng. Mater. 550 (2013): p. 115-125.
9. Y. Rong-xian, L. Zhi-yi, Y. Pu-you, L. Jun-lin, L. Liang-hua, Z. Su-min, Trans. Nonferrous Met. Soc. China 26 (2016): p. 1183-1190.
10. N.D. Alexopoulos, Z. Velonaki, C.I. Stergiou, S.K. Kourkoulis, Mater. Sci. Eng. A 700 (2017): p. 457-467.
11. I.M. Astika, IOP Conf. Ser. Mater. Sci. Eng. 539 (2019): article 012004.
12. Z. Wang, M. Chen, H. Jiang, H. Li, Song Li, Mater. Charact. 165 (2020): article 110383.
13. X. Xu, Y. Deng, S. Chi, X. Guo, J. Mater. Res. Technol. 9 (2020): p. 230-241.

14. K. Pakravan, A.H. Monazzah, S. Farahmand, Mater. Res. Express 7 (2020): article 056522.
15. Y.H. Zhao, X.Z. Liao, S. Cheng, E. Ma, Y.T. Zhu, Adv. Mater. 18 (2006): p. 2280-2283.
16. S.P. Knight, M. Salagaras, A.M. Wythe, F. De Carlo, A.R. Trueman, Corros. Sci. 52 (2010): p. 3855-3860.
17. R. Bonzom, R. Oltra, Corros. Sci. 111 (2016): p. 850-855.
18. Z. Wang, P. Chen, H. Li, B. Fang, Z. Zheng, Corros. Sci. 114 (2017): p. 156-168.
19. R. Davis, Corrosion of Aluminum and Aluminum Alloys (Materials Park, OH: ASM International, 1999).
20. J.O. Park, C.H. Paik, Y.H. Huang, R.C. Alkire, J. Electrochem. Soc. 146 (1999): p. 517-523.
21. A. Boag, R.J. Taylor, T.H. Muster, N. Goodman, D. McCulloch, C. Ryan, B. Rout, D. Jamieson, A.E. Hughes, Corros. Sci. 52 (2010): p. 90-103.
22. L. Lacroix, L. Ressier, C. Blanc, G. Mankowski, J. Electrochem. Soc. 155 (2008): p. 8-15.
23. M. Posada, L. E. Murr, C.-S. Niou, B. Roberson, D. Little, R. Arrowood, D. George, Mater. Charact. 38 (1997): p. 259-272.
24. M.J. Robinson, N.C. Jackson, Corros. Sci. 41 (1999): p. 1013-1028.
25. ASTM G34, "Standard Test Method for Exfoliation Corrosion Susceptibility in 2XXX and 7XXX Series Aluminum Alloys (EXCO Test)" (West Conshohocken, PA: ASTM International, 2001).
26. M.J. Robinson, N.C. Jackson, Br. Corros. J. 34, 1 (1999): p. 45-49.
27. M.J. Robinson, Corros. Sci. 22, 8 (1982): p. 775-790.
28. D.J. Kelly, M.J. Robinson, Corrosion 49, 10 (1993): p. 787-795.
29. Al. Th. Kermanidis, P.V. Petroyiannis, Sp. G. Pantelakis, Theor. Appl. Fract. Mech. 43 (2005): p. 121-132.
30. M. Guérin, J. Alexis, E. Andrieu, C. Blanc, G. Odemer, Mater. Des. 87 (2015): p. 681-692.
31. Y. Chen, C. Liu, J. Zhou, X. Wang, Int. J. Fatigue 98 (2017): p. 269-278.
32. K. Jones, D.W. Hoeppner, Corros. Sci. 48 (2006): p. 3109-3122.
33. Al.Th. Kermanidis, P.V. Petroyiannis, Sp.G. Pantelakis, Theor. Appl. Fract. Mech. 43 (2005): p. 121-132.
34. N.D. Alexopoulos, C.J. Dalakouras, P. Skarvelis, S.K. Kourkoulis, Corros. Sci. 55 (2012): p. 289-300.
35. Sp.G. Pantelakis, P.G. Daglaras, Ch.Alk. Apostolopoulos, Theor. Appl. Fract. Mech. 33 (2000): p. 117-134.
36. H. Kamoutsi, G.N. Haidemenopoulos, V. Bontozoglou, Sp.G. Pantelakis, Corros. Sci. 48 (2006): p. 1209-1224.
37. R.A. Causey, R.A. Karnesky, C. San Marchi, "Tritium Barriers and Tritium Diffusion in Fusion Reactors," in Comprehensive Nuclear Materials, eds. R.J.M. Konings, R.E. Stoller (Amsterdam, The Netherlands: Elsevier, 2012), p. 511-549.
38. C.E. Ransley, H. Neufeld, J. Inst. Met. 74 (1948): p. 599-620.
39. S. Kuramoto, J. Okahana, M. Kanno, Mater. Trans. 42 (2001): p. 2140-2143.
40. D.E. Azofeifa, N. Clark, A. Amador, A. Sáenz, Thin Solid Films 300 (1997): p. 295-298.
41. E. Charitidou, G. Papapolymerou, G.N. Haidemenopoulos, N. Hasiotis, V. Bontozoglou, Scr. Mater. 41 (1999): p. 1327-1332.
42. J. Yamabe, T. Awane, Y. Murakami, Int. J. Hydrogen Energy 42 (2017): p. 24560-24568.
43. H. Kamoutsi, G.N. Haidemenopoulos, V. Bontozoglou, P.V. Petroyiannis, S. G. Pantelakis, Corros. Sci. 80 (2014): p. 139-142.
44. G.A. Young, J.R. Scully, Acta Mater. 46 (1998): p. 6337-6349.

45. G.M. Bond, I.M. Robertson, H.K. Birnbaum, Acta Metall. 359 (1987): p. 2289-2296.
46. H.K. Birnbaum, P. Sofronis, Mater. Sci. Eng. A 176 (1994): p. 191-202.
47. C.D. Beachem, Metall. Trans. A 3 (1972): p. 441-455.

48. A.R. Troiano, Trans ASM 52 (1960): p. 54-80.
49. N.D. Alexopoulos, C. Charalampidou, P. Skarvelis, S.K. Kourkoulis, Corros. Sci. 121 (2017): p. 32-42.
50. ASTM E8M, "Standard Test Methods for Tension Testing of Metallic Materials" (West Conshohocken, PA: ASTM International, 2009).
51. ASTM E561, "Standard Practice for R-Curve Determination" (West Conshohocken, PA: ASTM International, 1998).
52. ASTM G44, "Exposure of Metals and Alloys by Alternate Immersion in Neutral 3.5% Sodium Chloride Solution" (West Conshohocken, PA: ASTM International, 2005).
53. ASTM E 1681, "Standard Test Method for Determining Threshold Stress Intensity Factor for Environment-Assisted Cracking of Metallic Materials" (West Conshohocken, PA: ASTM International, 1999).
54. ASTM E1820, "Standard Practice for Measurement of Fracture Toughness" (West Conshohocken, PA: ASTM International, 2001).
55. N.D. Alexopoulos, N. Siskou, C.-M. Charalampidou, S.K. Kourkoulis, Frattura ed Integrità Strutturale 50 (2019): p. 342-353.
56. S.P. Knight, M. Salagaras, A.R. Trueman, Corros. Sci. 53 (2011): p. 727-734.
57. H. Kamoutsi, "Corrosion Induced Hydrogen Embrittlement In High Strength Al Alloys," (Ph.D. thesis diss., University of Thessaly, Volos, Greece, 2004).
58. Sp.G. Pantelakis, D. Setsika, A. Chamos, A. Zervaki, Int. J. Struct. Integr. 7 (2016): p. 25-46.
59. C. Charalampidou, W. Dietzel, M. Zheludkevich, S.K. Kourkoulis, N.D. Alexopoulos, Corros. Sci. 183 (2021): p. 109330.
60. A.E. Hughes, A. Boag, A.M. Glenn, D. McCulloch, T.H. Muster, C. Ryan, C. Luo, X. Zhou, G.E. Thompson, Corros. Sci. 53 (2011): p. 27.
61. C. Luo, X. Zhou, G.E. Thompson, A.E. Hughes, Corros. Sci. 61 (2012): p. 35-44.
62. C. Vargel, "2.2.1. Initiation and Propagation of Corrosion Pits," in Corrosion of Aluminium, 1st ed. (Amsterdam, The Netherlands: Elsevier Science, 2004), p. 115-116.
63. K.H. Gayer, L.C. Thompson, O.T. Zajicek, Can. J. Chem. 36 (1958): p. 1268-1271.
64. X. Zhanga, Y. Jiao, Y. Yu, B. Liu, T. Hashimoto, H. Liu, Z. Dong, Corros. Sci. 155 (2019): p. 1-12.